

part of numerous theoretical treatments of the physics of high-temperature superconductors, in both the normal and superconducting states, but until now their presence had never been directly confirmed experimentally. This locally non-dispersive structure has been invoked, for example, to explain the striking differences observed between the in-plane and out-of-plane normal state conductivities  $\sigma_{ab}(\omega, T)$  and  $\sigma_{\perp}(\omega, T)$  (refs 5, 6). In the superconducting state, these  $t_{\perp}(\phi)$  zeros coincide precisely with nodes in the  $d$ -wave order parameter<sup>27</sup>. This vanishing of  $c$ -axis tunnelling right at the gap nodes is thought to be responsible for the striking differences in the  $T$ -dependencies of the in-plane and out-of-plane penetration depths  $\lambda_{ab}(T)$  and  $\lambda_{\perp}(T)$  (ref. 7), the absence of the zero-bias conductance peak inside the  $d$ -wave vortex core<sup>8</sup> and the slowly decaying tails in the tunnelling conductance around each vortex<sup>9</sup>.

Finally, the experimental demonstration of the existence of a 3D coherent FS in Tl2201 represents a significant challenge to models of high- $T_c$  superconductivity based on purely 2D electron motion within the CuO<sub>2</sub> planes. Although Tl2201 at this level of doping clearly comes from the side of the phase diagram in which more conventional behaviour is observed<sup>28</sup>, it is still a high-temperature superconductor ( $T_c \approx 20$  K). Moreover, its normal state resistive anisotropy ( $\rho_{\perp}/\rho_{ab} \approx 1,000$ ; ref. 16) is actually larger than that seen in some optimally doped materials, so it seems likely that the findings reported here will apply to a wider range of dopings. In common with other studies of Tl2201 (ref. 29), this work supports a model of the normal state based around fermionic quasiparticles. How and where this model breaks down as the Mott insulator is approached at half-filling of course remains an important outstanding issue. However, in providing crucial information on the dimensionality of the conducting planes, AMRO may prove to become an ideal complementary probe to ARPES in exploring this evolution of the electronic ground state in copper oxides across the phase diagram. □

Received 7 May; accepted 7 August 2003; doi:10.1038/nature01981.

1. Ong, N. P. Non-Fermi-liquid aspects of charge-transport in cuprate superconductors. *Physica C* **235**, 221–224 (1994).
2. Orenstein, J. & Millis, A. J. Advances in the physics of high temperature superconductivity. *Science* **288**, 468–474 (2000).
3. Yamaji, K. On the angle dependence of the magnetoresistance in quasi-two-dimensional organic superconductors. *J. Phys. Soc. Jpn* **58**, 1520–1522 (1989).
4. Andersen, O. K., Liechtenstein, A. I., Jepsen, O. & Paulsen, F. LDA energy bands, low-energy Hamiltonians  $t'$ ,  $t''$ ,  $t_{\perp}(k)$  and  $J_{\perp}$ . *J. Phys. Chem. Solids* **56**, 1573–1591 (1995).
5. Ioffe, L. B. & Millis, A. J. Zone-diagonal-dominated transport in high- $T_c$  cuprates. *Phys. Rev. B* **58**, 11631–11637 (1998).
6. van der Marel, D. Anisotropy of the optical conductivity of high- $T_c$  cuprates. *Phys. Rev. B* **60**, R765–R769 (1999).
7. Xiang, T. & Wheatley, J. M.  $c$ -axis superfluid response of copper oxide superconductors. *Phys. Rev. Lett.* **76**, 4632–4635 (1996).
8. Wu, C., Xiang, T. & Su, Z.-B. Absence of the zero bias peak in vortex tunneling spectra of high-temperature superconductors. *Phys. Rev. B* **62**, 14427–14430 (2000).
9. Franz, M. & Tesanovic, Z. Quasiparticle spectra in the vicinity of a  $d$ -wave vortex. *Phys. Rev. B* **60**, 3581–3588 (1999).
10. Kartsovnik, M. V., Laukhin, V. N., Pesotskii, S. I., Schegolev, I. F. & Yakovenko, V. M. Angular magnetoresistance oscillations and the shape of the Fermi surface in  $\beta$ -(ET)<sub>2</sub>IBr<sub>2</sub>. *J. Phys. I* **2**, 89–99 (1992).
11. Wosnitza, J. *et al.* The Fermi surfaces of  $\beta$ -(BEDT-TTF)<sub>2</sub>X. *J. Phys. I* **6**, 1597–1608 (1996).
12. Mackenzie, A. P., Julian, S. R., Sinclair, D. C. & Lin, C. T. Normal state magnetotransport in superconducting Tl<sub>2</sub>Ba<sub>2</sub>CuO<sub>6+ $\delta$</sub>  to millikelvin temperatures. *Phys. Rev. B* **53**, 5848–5854 (1996).
13. Tyler, A. W. *An Investigation into the Magnetotransport Properties of Layered Superconducting Perovskites*. Thesis, Univ. Cambridge (1997).
14. Tyler, A. W. *et al.* High field study of normal state magnetotransport in Tl<sub>2</sub>Ba<sub>2</sub>CuO<sub>6+ $\delta$</sub> . *Phys. Rev. B* **57**, R728–R731 (1998).
15. Mackenzie, A. P. *et al.* Resistance upper critical field in Tl<sub>2</sub>Ba<sub>2</sub>CuO<sub>6</sub> at low temperatures and high magnetic fields. *Phys. Rev. Lett.* **71**, 1238–1241 (1993).
16. Hussey, N. E. *et al.* Angular dependence of the  $c$ -axis normal state magnetoresistance in single crystal Tl<sub>2</sub>Ba<sub>2</sub>CuO<sub>6+ $\delta$</sub> . *Phys. Rev. Lett.* **76**, 122–125 (1996).
17. Dragulescu, A., Yakovenko, V. M. & Singh, D. J. Theory of angular magnetoresistance oscillations in Tl<sub>2</sub>Ba<sub>2</sub>CuO<sub>6</sub>. *Phys. Rev. B* **60**, 6312–6315 (1999).
18. Singh, D. J. & Pickett, W. E. Electronic characteristics of Tl<sub>2</sub>Ba<sub>2</sub>CuO<sub>6</sub>. *Physica C* **203**, 193–199 (1992).
19. Bergemann, C., Julian, S. R., Mackenzie, A. P., NishiZaki, S. & Maeno, Y. Detailed topography of the Fermi surface of Sr<sub>2</sub>RuO<sub>4</sub>. *Phys. Rev. Lett.* **84**, 2662–2665 (2000).
20. Ziman, J. M. *Principles of the Theory of Solids* (Cambridge Univ. Press, Cambridge, 1972).
21. Pavarini, E., Dasgupta, I., Saha-Dasgupta, T., Jepsen, O. & Andersen, O. K. Band-structure trend in hole-doped cuprates and correlation with  $T_{\text{max}}$ . *Phys. Rev. Lett.* **87**, 047003 (2001).

22. McKenzie, R. H. & Moses, P. Incoherent interlayer transport and angular-dependent magnetoresistance oscillations in layered metals. *Phys. Rev. Lett.* **81**, 4492–4495 (1998).
23. Kumar, N. & Jayannavar, A. M. Temperature dependence of the  $c$ -axis resistivity of high- $T_c$  layered oxides. *Phys. Rev. B* **45**, 5001–5004 (1992).
24. Tamasaku, K., Ito, T., Takagi, H. & Uchida, S. Interplane charge dynamics in La<sub>2-x</sub>Sr<sub>x</sub>CuO<sub>4</sub>. *Phys. Rev. Lett.* **72**, 3088–3091 (1994).
25. Damascelli, A., Hussain, Z. & Shen, Z.-X. Angle-resolved photoemission studies of the cuprate superconductors. *Rev. Mod. Phys.* **75**, 473–541 (2003).
26. Hussey, N. E. The normal state scattering rate in high- $T_c$  cuprates. *Eur. Phys. J. B* **31**, 495–507 (2003).
27. Hussey, N. E. Low-energy quasi-particles in high- $T_c$  cuprates. *Adv. Phys.* **51**, 1685–1771 (2002).
28. Nakamae, S. *et al.* Electronic ground state of heavily overdoped non-superconducting La<sub>2-x</sub>Sr<sub>x</sub>CuO<sub>4</sub>. *Phys. Rev. B* **68**, 100502 (2003).
29. Proust, C., Boaknin, E., Hill, R. W., Taillefer, L. & Mackenzie, A. P. Heat transport in a strongly overdoped cuprate: Fermi liquid and a pure  $d$ -wave BCS superconductor. *Phys. Rev. Lett.* **89**, 147003 (2002).
30. Bergemann, C. *et al.* Quasi-two-dimensional Fermi liquid properties of the unconventional superconductor Sr<sub>2</sub>RuO<sub>4</sub>. *Adv. Phys.* (in the press).

**Acknowledgements** We acknowledge technical support from S. Hannahs, and discussions with O. K. Andersen, C. Bergemann, S. J. Blundell, B. L. Györfy, R. Hlubina, A. J. Leggett, G. Santi and J. A. Wilson. We also acknowledge J. R. Cooper for first recognizing the potential of AMRO studies in Tl2201. This work was supported by EPSRC, the Leverhulme Trust and by a cooperative agreement between the State of Florida and NSF. The crystals were grown by A.P.M., the experiments carried out by M.A.-J., L.B., A.C. and N.E.H., and the analysis performed by M.A.-J. and N.E.H. in discussion with A.P.M.

**Competing interests statement** The authors declare that they have no competing financial interests.

**Correspondence** and requests for materials should be addressed to N.E.H. (n.e.hussey@bristol.ac.uk).

## A broadband superconducting detector suitable for use in large arrays

Peter K. Day<sup>1</sup>, Henry G. LeDuc<sup>1</sup>, Benjamin A. Mazin<sup>2</sup>, Anastasios Vayonakis<sup>2</sup> & Jonas Zmuidzinas<sup>2</sup>

<sup>1</sup>Jet Propulsion Laboratory, Pasadena, California 91107, USA

<sup>2</sup>California Institute of Technology, 320-47, Pasadena, California 91125, USA

Cryogenic detectors are extremely sensitive and have a wide variety of applications<sup>1–3</sup> (particularly in astronomy<sup>4–8</sup>), but are difficult to integrate into large arrays like a modern CCD (charge-coupled device) camera. As current detectors of the cosmic microwave background (CMB) already have sensitivities comparable to the noise arising from the random arrival of CMB photons, the further gains in sensitivity needed to probe the very early Universe will have to arise from large arrays. A similar situation is encountered at other wavelengths. Single-pixel X-ray detectors now have a resolving power of  $\Delta E < 5$  eV for single 6-keV photons, and future X-ray astronomy missions<sup>7</sup> anticipate the need for 1,000-pixel arrays. Here we report the demonstration of a superconducting detector that is easily fabricated and can readily be incorporated into such an array. Its sensitivity is already within an order of magnitude of that needed for CMB observations, and its energy resolution is similarly close to the targets required for future X-ray astronomy missions.

Among cryogenic detectors, superconducting detectors are especially attractive because thin-film deposition and lithographic patterning techniques may be used to produce large arrays. Several types have been demonstrated, including tunnel junction detectors<sup>4,9,10</sup> and transition-edge sensors<sup>11</sup>. These have nearly achieved the desired performance<sup>5,6,8,12–14</sup> for energy-resolved detection of individual optical/ultraviolet/X-ray photons and sensitive power detection at millimetre and submillimetre wavelengths. However,

these detectors have generally been used with individual preamplifiers and wiring for the output signals, which is clearly impractical for large arrays. Instead, a multiplexed readout approach is needed, in which preamplifiers and signal wiring are shared among multiple detectors. Multiplexing schemes are now being developed for transition-edge sensors<sup>15,16</sup>, but will require complex, custom-designed superconducting electronics, located close to the detector array. Our detector concept<sup>17</sup> is based on the microwave measurement of the complex impedance of a thin superconducting film, and allows a simple frequency-domain approach to multiplexing. This results in a dramatic simplification of the detector array and associated cryogenic electronics, and harnesses the rapid advances in wireless communications electronics. The results we present include the demonstration of single X-ray photon detection with a high signal-to-noise ratio and a measurement of the detector noise. Although much work remains to be done to optimize the performance, and to produce and use practical detector arrays, the devices already achieve very interesting levels of sensitivity.

In order to explain the operation of our detector, we must quickly review the electrodynamics of superconductors<sup>18</sup>. As its name implies, a superconductor has zero resistance for d.c. electrical

current. This supercurrent is carried by pairs of electrons, known as Cooper pairs. Cooper pairs are bound together by the electron-phonon interaction, with a binding energy  $2\Delta \approx 3.5k_B T_c$ , where  $T_c$  is the superconducting transition temperature. However, superconductors have a nonzero impedance for a.c. currents. An electric field applied near the surface of a superconductor causes the Cooper pairs to accelerate, allowing energy storage in the form of kinetic energy. Because the supercurrent is non-dissipative, this energy may be extracted by reversing the electric field. Similarly, energy may be stored in the magnetic field inside the superconductor, which penetrates only a short distance,  $\lambda \approx 50$  nm, from the surface. The overall effect is that a superconductor has a surface inductance  $L_s = \mu_0 \lambda$ , due to the reactive energy flow between the superconductor and the electromagnetic field. The surface impedance  $Z_s = R_s + i\omega L_s$  also includes a surface resistance  $R_s$ , which describes a.c. losses at angular frequency  $\omega$  caused by the small fraction of electrons that are not in Cooper pairs, which are called 'quasiparticles'. For temperatures  $T$  much lower than  $T_c$ ,  $R_s \ll \omega L_s$ .

Photons with sufficient energy ( $h\nu > 2\Delta$ ) may break apart one or more Cooper pairs (Fig. 1a). The absorption of a high-energy photon creates  $N_{qp} \approx \eta h\nu / \Delta$  quasiparticles; the excess quasiparti-

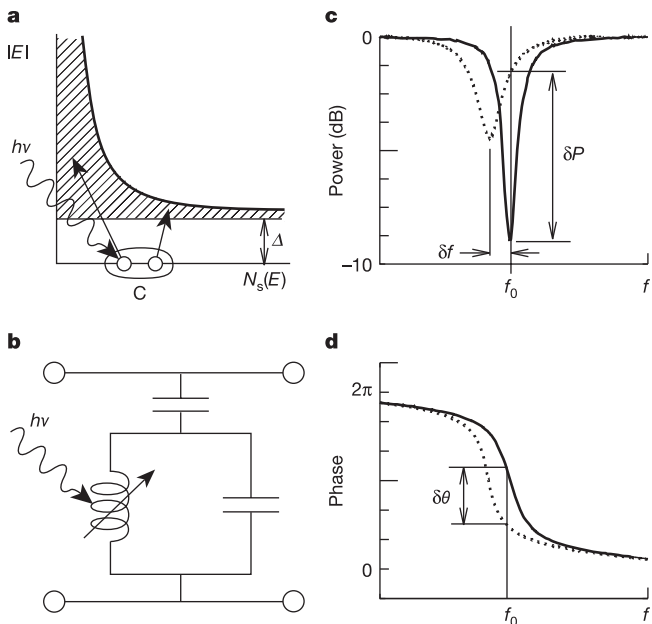


**Figure 1** An illustration of the detection principle. **a**, Photons with energy  $h\nu > 2\Delta$  are absorbed in a superconducting film cooled to  $T \ll T_c$ , breaking Cooper pairs and creating a number of quasiparticle excitations  $N_{qp} = \eta h\nu / \Delta$ . In this diagram, Cooper pairs (C) are shown at the Fermi level, and the density of states for quasiparticles<sup>18</sup>,  $N_s(E)$ , is plotted as the shaded area as a function of quasiparticle energy  $E$ . **b**, The increase in quasiparticle density changes the (mainly inductive) surface impedance  $Z_s = R_s + i\omega L_s$  of the film, which is used as part of a microwave resonant circuit. The resonant circuit is depicted schematically here as a parallel LC circuit which is capacitively coupled to a through line. The effect of the surface inductance  $L_s$  is to increase the total inductance  $L$ , while the effect of the surface resistance  $R_s$  is to make the inductor slightly lossy (adding a series resistance). **c**, On resonance, the LC circuit loads the through line, producing a dip in its transmission. The quasiparticles produced by the photons increase both  $L_s$  and  $R_s$ , which moves the resonance to lower frequency (due to  $L_s$ ), and makes the dip broader and shallower (due to  $R_s$ ). Both of these effects contribute to changing the amplitude (producing power change  $\delta P$ ) (**c**) and phase (**d**) of a microwave probe signal transmitted through the circuit. The definition of the phase angle used here is explained in Fig. 3. The amplitude and phase curves shown in this illustration are actually the data measured for the test device (Fig. 2) at 120 mK (solid lines) and 260 mK (dashed lines). This choice of circuit design, which has high transmission away from resonance, is very well suited for frequency-domain multiplexing, because multiple resonators operating at slightly different frequencies could all be coupled to the same through line.

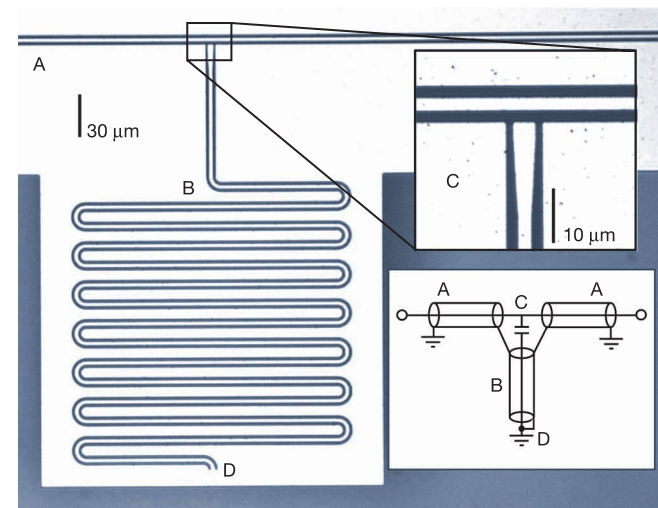


**Figure 2** A microscope photograph of the device tested. Light and dark regions are the aluminium film and bare sapphire substrate, respectively. A, coplanar waveguide (CPW) through line used for excitation and readout. B, Meandered quarter-wavelength resonator section, with an overall length of 3 mm, and resonance frequency around 10 GHz. C, coupling capacitor. D, short-circuit termination. The coupling region is magnified in the inset; the diagram shows the equivalent circuit. Both CPW lines have a  $50 \Omega$  characteristic impedance, and are fabricated from a single 2,200-Å-thick aluminium film ( $T_c = 1.23$  K) using standard contact photolithography. The centre conductor of width  $3 \mu\text{m}$  is separated by  $2\text{-}\mu\text{m}$  gaps from ground planes on either side. The fraction  $\alpha$  of the total inductance per unit length contributed by the surface inductance of the aluminium film can be written as a sum of centre strip and ground plane terms,  $\alpha = \alpha_{\text{centre}} + \alpha_{\text{ground}}$ . These are calculated to be  $\alpha_{\text{centre}} \approx 0.04$  and  $\alpha_{\text{ground}} \approx 0.02$  using a finite-element method<sup>26</sup>, assuming an effective penetration depth  $\lambda = 50$  nm. The measured resonator quality factor  $Q = f_0 / \Delta f$  is 52,500 at low temperatures  $T \ll T_c$  (Fig. 1). This device is mainly sensitive to photon events in the centre strip ( $V = 2,000 \mu\text{m}^3$ ) of the CPW line rather than in the ground plane, because the microwave current in the ground plane is concentrated near the edge of the CPW line; quasiparticles generated in the ground plane near the edge of the CPW line can easily diffuse away. Similarly, the device is more sensitive to centre strip events occurring near the short-circuited end, where the standing-wave pattern of the microwave current reaches a maximum. Quasiparticles generated in the centre strip may also diffuse out of the short-circuited end; the peak response therefore occurs roughly one diffusion length ( $\sim 1$  mm) from this end. Photon events in the through line are not seen, because there is no resonant enhancement of the surface impedance effect.

cles subsequently recombine into Cooper pairs on timescales  $\tau_{qp} \approx 10^{-3}$ – $10^{-6}$  s. Here  $\eta \approx 0.57$  is the efficiency with which the photon energy is converted to quasiparticles<sup>19</sup>. During this time, the quasiparticles can diffuse over a distance of  $l \approx \sqrt{D\tau_{qp}}$ , where  $D$  is the diffusion constant of the material. Similarly, the absorption of a steady stream of low-energy (millimetre/submillimetre) photons would raise the steady-state quasiparticle density by an amount  $\delta n_{qp}$  above its thermal equilibrium value. Our detectors make use of the dependence of the surface impedance  $Z_s$  on quasiparticle density. Although the changes  $\delta Z_s$  are quite small, very sensitive measurements may be made using a resonant circuit (Fig. 1b). Changes in  $L_s$  and  $R_s$  affect the frequency and width of the resonance, respectively, changing the amplitude and phase of a microwave signal transmitted through the circuit (Fig. 1c and d).

The change in surface impedance  $\delta Z_s$  may be expressed as  $\delta Z_s = \delta n_{qp} \partial Z_s / \partial n_{qp}$ , where the derivative depends on  $\omega$ ,  $T$ , and material parameters, and may be calculated using the Mattis–Bardeen theory<sup>20</sup>. Very crudely, we expect the fractional surface impedance change to be comparable to the fraction of Cooper pairs that are broken. This leads to the estimate  $\delta L_s / L_s \approx \delta n_{qp} / 2N_0 \Delta$ , where  $N_0$  is the single spin density of states at the Fermi level, as  $N_0 \Delta$  can be thought of as the density of Cooper pairs. The resulting fractional change in the resonance frequency  $f_0$  is  $|\delta f| / f_0 = 0.5 \alpha \delta L_s / L_s$ , where

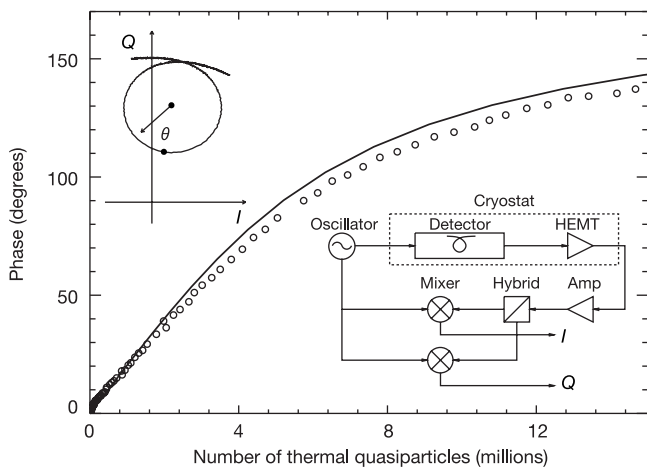


**Figure 3** The microwave measurement set-up and the phase calibration of the detector. A low-phase noise microwave synthesizer (right inset) generates the fixed-frequency signal used to excite the detector, which is cooled in a dilution refrigerator. After transmission through the device, the signal is amplified by a broadband cryogenic HEMT amplifier with  $\sim 50$  K noise temperature (including cable loss) and a room-temperature amplifier. An  $I/Q$  (inphase-quadrature) mixer is used to measure the amplitude and phase of the transmitted signal as a function of time. The left inset shows the measured resonance trajectory as a function of frequency in the  $I/Q$  plane (in arbitrary units), at 120 mK. The point plotted on the resonance circle indicates the resonance frequency. As shown by the arrow, the phase angle,  $\theta$ , is calculated relative to this point using the centre of the circle as the reference. At low quasiparticle densities, this phase angle depends only on  $L_s$  and is proportional to the actual microwave phase shift through the device. The points on the main plot show the measured phase angle,  $\theta$ , as a function of the calculated number of thermal quasiparticles in the central conductor of the resonator,  $N_{qp}(T) = n_{qp} V = 2N_0 V (2\pi k_B T \Delta)^{1/2} \exp(-\Delta/k_B T)$ , obtained by varying the temperature  $T$ . Here  $N_0 = 1.72 \times 10^{10} \mu\text{m}^{-3} \text{eV}^{-1}$  is the single-spin density of states at the Fermi surface, including the electron–phonon enhancement factor<sup>27</sup>. The line gives the phase calculated from theory for  $\alpha = 0.061$  (Fig. 2),  $\Delta = 0.171$  meV,  $Q(T=0) = 52,500$  (limited by coupling), and assuming the Mattis–Bardeen theory<sup>20</sup> for  $Z_s$  in the extreme anomalous limit (as  $\xi_0 \approx 1,600$  nm  $\gg \lambda_0 = 16$  nm for aluminium). The value of  $\Delta$  is in reasonable agreement<sup>28</sup> with the measured  $T_c = 1.23$  K. These parameter values also reproduce the measured temperature dependence of the frequency shift  $\delta f(T) = f(T) - f(0)$  and quality factor  $Q(T)$  of the resonance, according to  $\delta f(T)/f(0) = -\alpha \delta L_s(T)/2L_s(0)$  and  $Q^{-1}(T) = Q^{-1}(0) + \alpha R_s(T)/\omega L_s(0)$ .

$\alpha$  is the fraction of the circuit inductance that is contributed by the surface inductance  $L_s$ . For our test device (Fig. 2), which has  $\alpha \approx 0.04$ ,  $V = 2,000 \mu\text{m}^3$  and  $\Delta \approx 0.171$  meV (Fig. 3), we expect  $|\delta f|/f_0 \approx 5 \times 10^{-5}$  when a single 5.9-keV X-ray photon is absorbed (Fig. 4). This frequency shift should be compared against the width of the resonance, which is  $\Delta f/f_0 = Q^{-1} = 2 \times 10^{-5}$ , as the quality factor of our test device is  $Q = 52,500$  at low temperatures. Thus, we conclude that single 5.9-keV X-ray photons should easily be detectable, driving the resonator nearly off-resonance, and producing large phase shifts of the order of  $180^\circ$ . In fact, this is what is observed (Fig. 4). In this example, the fraction of Cooper pairs that are broken is quite small, of the order of  $2 \times 10^{-3}$ . This allows us to regard the derivative  $\partial Z_s / \partial n_{qp}$  as being essentially constant.

We studied a device with a quarter-wavelength transmission line resonator (Fig. 2). This circuit is the transmission line equivalent of the lumped element resonator shown in Fig. 1b. A homodyne detection scheme (Fig. 3, right inset) is used to measure the transmission amplitude and phase at the resonance frequency as a function of time. We convert the time-dependent transmission measurements into a phase angle,  $\theta(t)$ , as indicated in Fig. 3 (left inset). Figure 3 shows the measured and calculated phase angle versus  $N_{qp}$ , the total number of quasiparticles in the centre strip of the coplanar waveguide (CPW) line, obtained by varying the

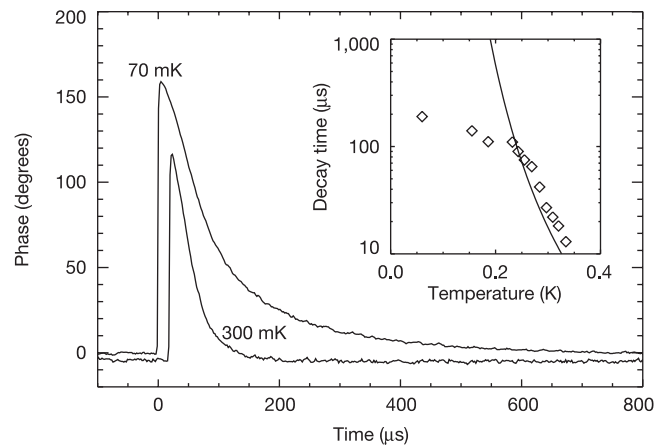


**Figure 4** Single-photon X-ray pulses measured at 70 and 300 mK. The phase is calculated from the time-domain  $I/Q$  data (Fig. 3). The data points are taken at 2- $\mu\text{s}$  intervals and are statistically independent. To compare pulse heights from absorption events in the centre strip to the thermal calibration of Fig. 3, we should multiply by  $\alpha_{\text{centre}}/\alpha \approx 0.66$ . On the other hand, the thermal quasiparticles are distributed uniformly throughout the device, whereas the largest X-ray events will be those from X-rays absorbed near the sensitive shorted end. These two effects approximately cancel. A simple exponential decay does not describe the pulses well, except in the tails. In the inset, we compare the decay times measured using the tails of the pulses to the theoretical quasiparticle recombination time (solid line),  $\tau_{\text{rec}}$ , calculated by Kaplan<sup>29</sup>. At high temperatures the measured decay times lie above the theoretical curve, but have a similar temperature dependence, whereas at low temperatures the measured decay times saturate. The measured decay times are expected to be larger than  $\tau_{\text{rec}}$  owing to phonon trapping. The saturation could have a number of explanations: for example, an excess background quasiparticle population due to stray radiation; or trapping and recombination at defects, grain boundaries, or fluxons (due to Earth’s field), where the gap parameter is reduced. Quasiparticles may also diffuse out of the centre strip through the shorted end of the resonator. The average diffusion length before recombination can be expected to be of the order of 1 mm. If the decay time saturation is due to excess background quasiparticles, we estimate  $N_{qp} \approx 2 \times 10^6$  by calculating the thermal density at the saturation temperature. This value of  $N_{qp}$  would not significantly modify the coupling-limited low-temperature  $Q$  of the resonator, but is approximately consistent with an estimate of the internal resonator loss obtained using the depth of the transmission dip.

temperature. The responsivity  $\partial\theta/N_{qp}$  is fairly constant for low quasiparticle concentrations, when  $Q$  is close to its low-temperature limit  $Q(0)$ . At higher quasiparticle densities, the phase responsivity decreases as the resonance moves off the excitation frequency and becomes broader.

We investigated the photoresponse of the device using an  $^{55}\text{Fe}$  source, which emits 5.9-keV X-rays. Pulses of various amplitudes are observed, as expected, as the resonator has a position-dependent response owing to the standing-wave current distribution. Quasiparticle outdiffusion also plays a role (Fig. 2). The largest events are identified with hits on the centre strip near the shorted end. Sample X-ray events of this type measured at 70 mK and 300 mK are shown in Fig. 4. The X-rays create approximately  $^{19}\eta E_{xray}/\Delta \approx 2 \times 10^7$  quasiparticles, which should saturate the detector (Fig. 3) and produce a peak phase shift approaching  $180^\circ$ , as observed.

We can estimate the noise equivalent power (NEP) of the detector as a function of frequency  $\omega$  using the measured phase noise power spectrum  $S_\theta(\omega)$  along with the measured responsivity  $\partial\theta/\partial N_{qp}$  (Fig. 3):

$$\text{NEP}^2(\omega) = S_\theta(\omega) \left( \frac{\eta\tau_0}{\Delta} \frac{\partial\theta}{\partial N_{qp}} \right)^{-2} (1 + \omega^2\tau_0^2) \quad (1)$$

where  $\tau_0$ , the response time of the detector, is determined from the pulse tails. Figure 5 shows the estimated NEP at 100 mK, and the

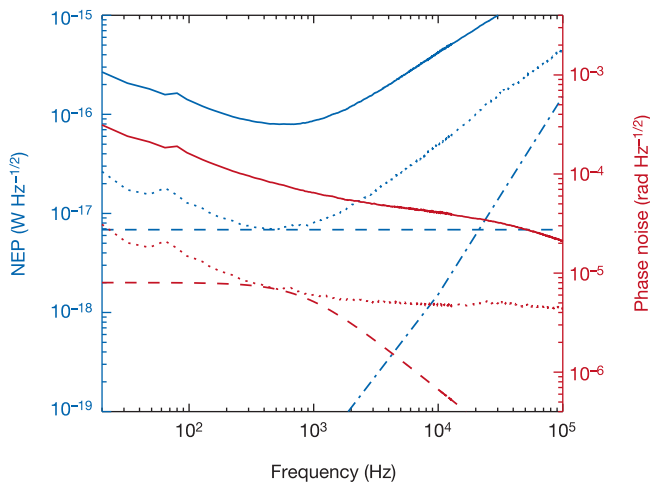


**Figure 5** A plot of the noise measured for the test device; several other devices have given similar results. The right axis (red curves) gives the total output phase noise spectrum  $S_\theta^{1/2}(\omega)$ , while the left axis (blue curves) show noise equivalent power, NEP as described in the text. The solid lines give the total noise, and the dotted lines give the estimated contribution from the HEMT amplifier, measured by tuning the excitation frequency off resonance. The NEP values are applicable for absorbed power levels low enough that  $\tau_0$  and  $\partial\theta/\partial N_{qp}$  are not changed. The dashed lines give an upper bound to the generation-recombination noise, assuming a quasiparticle population of  $N_{qp} = 2 \times 10^6$  in the device, which is consistent with the measured saturation of pulse decay time (Fig. 4). The NEP contribution from the microwave synthesizer, estimated from its specifications, is shown as the dot-dashed line. At frequencies lower than  $\Delta\omega_r$ , the bandwidth of the resonator, synthesizer noise is suppressed by the factor  $\omega/\Delta\omega_r$ , because the resonator phase can track the synthesizer phase fluctuations within a bandwidth  $\Delta\omega_r$ . The estimated noise contributions appear to be at least 10 dB below the total measured noise, which indicates extra noise of unknown origin; the possibilities include random motion of fluxons trapped in the superconducting films, stray radiation with  $h\nu \gg \Delta$ , and substrate noise. These may be experimentally investigated by using magnetic shielding, improving the filtering for the microwave coaxial lines in the cryostat, and by varying the device geometry, materials, substrate, and so on. The amplifier noise should not be a limiting factor. Gain and phase fluctuations may be eliminated using carrier suppression or other methods. For the present device, the amplifier white noise (50 K) limit is  $\Delta E = 1$  eV and  $\text{NEP} = 5 \times 10^{-18} \text{ W Hz}^{-1/2}$ , improving to 0.3 eV and  $2 \times 10^{-18} \text{ W Hz}^{-1/2}$  for an optimized 5 K amplifier.

estimated contributions of the amplifier and synthesizer phase noise. The energy resolution can be estimated<sup>21</sup> from  $\text{NEP}(\omega)$ , giving  $\Delta E = 11$  eV, which is consistent with the pulse signal-to-noise ratio. It is important to note that the present device cannot actually be used for spectroscopy at this resolution owing to its position-dependent response; a more sophisticated device will be needed (see below). Nonetheless, this result indicates the potential of the concept.

The intrinsic noise at  $T \ll T_c$  is expected to arise from random generation and recombination of quasiparticles<sup>22,23</sup>, which should be negligible at 100 mK if the quasiparticle population is thermal. Although it is possible that there are excess quasiparticles—for example, generated by stray radiation—limits may be set on this excess population using the observed saturation of  $\tau_0$  (Fig. 4), which in turn gives a generation-recombination NEP limit of  $6 \times 10^{-18} \text{ W Hz}^{-1/2}$  (Fig. 5). The measured noise appears to be larger than the estimated readout and intrinsic noise; this is clearly an important area for further research.

Frequency multiplexing is accomplished by coupling an array of many resonators with slightly different resonance frequencies to a common transmission line. A single cryogenic HEMT (high electron mobility transistor) amplifier is capable of amplifying the output signals from a large number of detectors, as many as  $10^3$ – $10^4$ , depending on the amplifier bandwidth and the detector frequency spacing. This depends on the  $Q$  and the lithographic control of the resonances. An array of synthesizers and quadrature receivers at room temperature completes the system, and is readily implemented using miniature, low-cost, low-power integrated circuits developed for wireless communications.

Practical detectors will require efficient coupling of photons or quasiparticles into the sensitive end of the resonators. Fortunately, methods developed for other types of superconducting detectors may be reused. Planar antennas with microstrip lines<sup>24</sup> work well at millimetre wavelengths, and tantalum superconducting films provide excellent optical/ultraviolet/X-ray quantum efficiency<sup>4,8,14</sup>. Diffusion and quasiparticle trapping<sup>14,25</sup> allow the separation of absorber and detector functions, which provides considerable flexibility for detector optimization.

Although the demonstrated performance is already good enough for some applications—such as ground-based submillimetre imaging—better sensitivity is desirable. What are the fundamental limits? The amplifier noise contribution can be substantially reduced (Fig. 5), to  $\text{NEP} \approx 10^{-18} \text{ W Hz}^{-1/2}$  for the present device. Further reductions of the readout noise will require a larger responsivity  $\partial\theta/N_{qp}$ , which is achievable by increasing  $Q$  or decreasing the volume; we have already measured  $Q = 2 \times 10^6$  for more weakly coupled devices. Similarly, the intrinsic generation-recombination noise does not set a hard sensitivity limit, as it decreases exponentially with temperature<sup>23</sup>. Thus, the potential exists to develop detectors with  $\text{NEP}$  below  $10^{-19} \text{ W Hz}^{-1/2}$ , which should be sufficient for most applications. The key issues for the future are understanding and reducing the noise sources in these devices, which we suspect are non-fundamental, and demonstrating efficient radiation coupling and multiplexing. □

Received 10 March; accepted 2 September 2003; doi:10.1038/nature02037.

1. Newbury, D. et al. The approaching revolution in X-ray microanalysis: The microcalorimeter energy dispersive spectrometer. *J. Radioanal. Nucl. Chem.* **244**, 627–635 (2000).
2. Booth, N., Cabrera, B. & Fiorini, E. Low-temperature particle detectors. *Annu. Rev. Nucl. Part. Sci.* **46**, 471–532 (1996).
3. Saab, T. et al. Deployment of the first CDMS II ZIP detectors at the Stanford Underground Facility. *Nucl. Phys. B* **110**, 100–102 (2002).
4. Peacock, A. et al. Single optical photon detection with a superconducting tunnel junction. *Nature* **381**, 135–137 (1996).
5. Cabrera, B. et al. Detection of single infrared, optical, and ultraviolet photons using superconducting transition edge sensors. *Appl. Phys. Lett.* **73**, 735–737 (1998).
6. Lee, S., Gildemeister, J., Holmes, W., Lee, A. & Richards, P. Voltage-biased superconducting transition-edge bolometer with strong electrothermal feedback operated at 370 mK. *Appl. Opt.* **37**, 3391–3397 (1998).
7. de Korte, P. Cryogenic imaging spectrometers for X-ray astronomy. *Nucl. Instrum. Meth. A* **444**(1–2),

163–169 (2000).

8. Rando, N. *et al.* S-cam: A spectrophotometer for optical astronomy: Performance and latest results. *Rev. Sci. Instrum.* **71**(12), 4582–4591 (2000).
9. Twerenbold, D. Giaever-type superconducting tunneling junctions as high-resolution X-ray-detectors. *Europhys. Lett.* **1**(5), 209–214 (1986).
10. Kraus, H. *et al.* High-resolution X-ray-detection with superconducting tunnel-junctions. *Europhys. Lett.* **1**(4), 161–166 (1986).
11. Irwin, K., Hilton, G., Wollman, D. & Martinis, J. X-ray detection using a superconducting transition-edge sensor microcalorimeter with electrothermal feedback. *Appl. Phys. Lett.* **69**(13), 1945–1947 (1996).
12. Irwin, K. *et al.* A Mo-Cu superconducting transition-edge microcalorimeter with 4.5 eV energy resolution at 6 keV. *Nucl. Instrum. Meth. A* **444**, 184–187 (2000).
13. Angloher, G. *et al.* Energy resolution of 12 eV at 5.9 keV from Al superconducting tunnel junction detectors. *J. Appl. Phys.* **89**, 1425–1429 (2001).
14. Li, L. *et al.* Improved energy resolution of X-ray single photon imaging spectrometers using superconducting tunnel junctions. *J. Appl. Phys.* **90**, 3645–3647 (2001).
15. Chervenak, J. *et al.* Superconducting multiplexer for arrays of transition edge sensors. *Appl. Phys. Lett.* **74**, 4043–4045 (1999).
16. Yoon, J. *et al.* Single superconducting quantum interference device multiplexer for arrays of low-temperature sensors. *Appl. Phys. Lett.* **78**, 371–373 (2001).
17. Mazin, B. A., Day, P. K., Leduc, H. G., Yayonakis, A. & Zmuidzinas, J. Superconducting kinetic inductance photon detectors. *Proc. SPIE* **4849**, 283–293 (2002).
18. Tinkham, M. *Introduction to Superconductivity*, 2nd edn (McGraw-Hill, New York, 1996).
19. Kozorezov, A. G. *et al.* Quasiparticle-phonon downconversion in nonequilibrium superconductors. *Phys. Rev. B* **61** (May), 11807–11819 (2000).
20. Mattis, D. C. & Bardeen, J. Theory of the anomalous skin effect in normal and superconducting metals. *Phys. Rev.* **111**, 412–417 (1958).
21. Moseley, S., Mather, J. & McCammon, D. Thermal detectors as x-ray spectrometers. *J. Appl. Phys.* **56**, 1257–1262 (1984).
22. Wilson, C., Frunzio, L. & Prober, D. Time-resolved measurements of thermodynamic fluctuations of the particle number in a nondegenerate Fermi gas. *Phys. Rev. Lett.* **87**, 067004 (2001).
23. Sergeev, A., Mitin, V. & Karasik, B. Ultrasensitive hot-electron kinetic-inductance detectors operating well below the superconducting transition. *Appl. Phys. Lett.* **80**, 817–819 (2002).
24. Zmuidzinas, J. & LeDuc, H. G. Quasi-optical slot antenna SIS mixers. *IEEE Trans. Microwave Theory Tech.* **MTT-40**, 1797–1804 (1992).
25. Li, L., Frunzio, L., Wilson, C. & Prober, D. Quasiparticle nonequilibrium dynamics in a superconducting Ta film. *J. Appl. Phys.* **93**, 1137–1141 (2003).
26. Chang, W. Inductance of a superconducting strip transmission-line. *J. Appl. Phys.* **50**, 8129–8134 (1979).
27. McMillan, W. Transition temperature of strong-coupled superconductors. *Phys. Rev.* **167**, 331–334 (1968).
28. Wells, G. L., Jackson, J. E. & Mitchell, E. N. Superconducting tunneling in single-crystal and polycrystal films of aluminum. *Phys. Rev. B* **1**, 3636–3644 (1970).
29. Kaplan, S. *et al.* Quasiparticle and phonon lifetimes in superconductors. *Phys. Rev. B* **14**, 4854–4873 (1976).

**Acknowledgements** This work has been supported in part by NASA (Aerospace Technology Enterprise), the JPL Director’s Research and Development Fund, and the Caltech President’s Fund. We are grateful for the support of A. Lidow, Caltech Trustee.

**Competing interests statement** The authors declare that they have no competing financial interests.

**Correspondence** and requests for materials should be addressed to P.K.D. (Peter.K.Day@jpl.nasa.gov).

## Imaging coexisting fluid domains in biomembrane models coupling curvature and line tension

Tobias Baumgart<sup>1</sup>, Samuel T. Hess<sup>2</sup> & Watt W. Webb<sup>1</sup>

<sup>1</sup>Applied and Engineering Physics, Cornell University, Ithaca, New York 14853, USA

<sup>2</sup>Laboratory of Cellular and Molecular Biophysics, National Institute of Child Health and Human Development, National Institutes of Health, Bethesda, Maryland 20892, USA

**Lipid bilayer membranes—ubiquitous in biological systems and closely associated with cell function—exhibit rich shape-transition behaviour, including bud formation<sup>1</sup> and vesicle fission<sup>2</sup>. Membranes formed from multiple lipid components can laterally separate into coexisting liquid phases, or domains, with distinct compositions. This process, which may resemble raft**

formation in cell membranes, has been directly observed in giant unilamellar vesicles<sup>3,4</sup>. Detailed theoretical frameworks<sup>5–11</sup> link the elasticity of domains and their boundary properties to the shape adopted by membranes and the formation of particular domain patterns, but it has been difficult to experimentally probe and validate these theories. Here we show that high-resolution fluorescence imaging using two dyes preferentially labelling different fluid phases directly provides a correlation between domain composition and local membrane curvature. Using freely suspended membranes of giant unilamellar vesicles, we are able to optically resolve curvature and line tension interactions of circular, stripe and ring domains. We observe long-range domain ordering in the form of locally parallel stripes and hexagonal arrays of circular domains, curvature-dependent domain sorting, and membrane fission into separate vesicles at domain boundaries. By analysing our observations using available membrane theory, we are able to provide experimental estimates of boundary tension between fluid bilayer domains.

We study giant unilamellar vesicles (GUVs) formed from a ternary mixture of the lipids sphingomyelin, dioleoylphosphatidylcholine (DOPC) and cholesterol<sup>3</sup>. Sphingomyelin and cholesterol enrich in a liquid phase with short-range order ( $L_o$ ), and DOPC prefers a disordered liquid ( $L_d$ ) phase. The phase diagram of this lipid mixture at physiologically relevant temperatures shows a large binary coexistence region of  $L_o$  and  $L_d$  domains (A.K. Smith and G.W. Feigenson, personal communication; see also Supplementary Information for further details). Figure 1 presents images of equatorial sections of GUVs (obtained using two-photon microscopy), exhibiting phase coexistence of the  $L_o$  (blue) +  $L_d$  (red) phases at varying compositions. Figure 1a–d and g, h shows shapes with symmetry around an axis in the vertical direction within the image plane.

The geometry of phase-separated vesicles is theoretically obtained by minimizing an energy functional with contributions arising from bending resistance, lateral tensions, line tension and normal pressure difference. The bending energy  $F_b$  of an axially symmetric lipid membrane has components arising from mean curvature (first term) and Gauss curvature<sup>12,13</sup> (second term), and is summed over every domain  $i$  of the vesicle<sup>8</sup>:

$$F_b^i = \frac{\kappa^i}{2} \int_{A^i} (C_m + C_p - C_0)^2 dA + \kappa_G^i \int_{A^i} C_m C_p dA \quad (1)$$

Here  $\kappa$ ,  $\kappa_G$ ,  $C_m$  and  $C_p$  are mean and Gauss bending rigidities and principal curvatures along the meridians and parallels, respectively, and the integral is extended over all domain areas  $i$ .  $C_0$  is a curvature preference, which is often assumed to be constant within a domain<sup>5,8,11</sup> but can in general vary locally<sup>14</sup>. The bending modulus  $\kappa$  typically has a value of  $\sim 10^{-19}$  J (ref. 15). The second term in equation (1) influences the vesicle shape only if  $\kappa_G^i$  values differ between domains  $i$  (ref. 8).

Comparison of Fig. 1a and 1b, which show similar shapes even though the domains are reversed, suggests that bending resistance differences (or any curvature preferences) are not dominant in determining global vesicle shapes. In fact, a line tension  $\sigma$  at the boundaries between coexisting fluid membrane domains has been proposed to control membrane deformation, budding and fission<sup>5</sup>. Theoretical estimates of  $\sigma$  are of the order of  $10^{-11}$  N for systems far from<sup>5</sup> critical points of the lipid phase diagram, and  $\sigma$  vanishes at critical points<sup>5,16</sup>. Above a limiting boundary length  $S^0 \approx 8\kappa/\sigma \approx 80$  nm, an initially flat domain would transform into a complete spherical bud with vanishing neck radius, provided that sufficient membrane area is available<sup>5</sup>. Accordingly, the domain boundary radii observed in Fig. 1 favour bud formation even for much smaller estimates of  $\sigma$ .

This simplifying theoretical description neglects the constraints on membrane domain areas and surface-to-volume ratio ( $s/v$ ), which are constant on the timescale of our experiment (up to